

Cite this: *Nanoscale*, 2014, 6, 13188

Nucleation kinetics of SrTiO₃ 3D islands and nanorings on Si substrates

Paloma Tejedor,^{*a} Marcos Benedicto,^a Luis Vázquez^a and Beatriz Galiana^b

The nucleation of SrTiO₃ three-dimensional (3D) islands and nanorings on Si substrates *via* a novel metal-organic decomposition (MOD) process has been investigated as a function of temperature and solution concentration of the SrTi(OC₃H₇)₆ precursor. Quantitative analysis of island density and size distribution by atomic force microscopy (AFM) has revealed the existence of a nucleation regime at solution concentrations below 5×10^{-3} M, in which the critical nucleus is a trimer and a coalescence regime at higher concentrations, dominated by growth of immobile clusters. Nanorings form preferentially under high supersaturation conditions and their size distribution is consistent with a dynamic coalescence. On the basis of recent theoretical models (Gill, 2012), we have proposed that the island-to-nanoring transition in the SrTiO₃/Si system occurs above a critical size as a result of a competition between energetic and kinetic factors. The combination of high-resolution transmission electron microscopy (HRTEM) and attenuated total reflectance Fourier transform infrared spectroscopy (ATR-FTIR) has shown that the monocrystalline SrTiO₃ nanoclusters grow pseudomorphically on the Si substrate and exhibit a strain-induced tetragonal lattice distortion.

Received 1st August 2014,
Accepted 28th August 2014

DOI: 10.1039/c4nr04416a

www.rsc.org/nanoscale

Introduction

The wide spectrum of functionalities observed in transition metal oxides belonging to the ABO₃ perovskite class originates from the possibility to control the size, shape and connectivity (*i.e.* distortion and rotation) of the corner-sharing BO₆ octahedral units.¹ Strontium titanate (SrTiO₃) in particular is one of the most versatile perovskite oxides, exhibiting exceptional electric, magnetic and thermal properties.² Recent reports demonstrate the ever-growing number of devices in which SrTiO₃ finds application: The use of metal-doped SrTiO₃ as an efficient UV photocatalyst electrode for water splitting,^{3,4} the suitability of undoped SrTiO₃ to serve as the insulator material in Ag/SrTiO₃/Pt resistance-change random access memory cells (RRAM), based on its bistable resistive switching effect,^{5,6} and the possibility to fabricate all-oxide electronic devices after the discovery of an anisotropic two-dimensional electron gas (2DEG) at the LaAlO₃–SrTiO₃ interface^{7–9} are just but a few examples.

Particularly relevant for the advance of complementary-metal-oxide-semiconductor (CMOS) technology is the growth of epitaxial SrTiO₃ on a Si (001) substrate^{10–16} to enable the fabrication of ferroelectric field-effect transistors (FeFETs) for

non-volatile memories and low-power logic applications^{17,18} or the monolithic integration of III–V semiconductors on Si.¹⁹ Bulk SrTiO₃ is not ferroelectric at any temperature, but the large compressive strain generated when a SrTiO₃ thin film is lattice-matched to the Si substrate induces a distortion in the cubic perovskite, which was predicted to result in ferroelectricity with an out-of-plane polarization²⁰ and later demonstrated for commensurately strained films grown by molecular beam epitaxy (MBE) below a certain critical thickness.¹⁴ The fabrication of highly-scaled perovskite-based ferroelectric devices, however, remains a mayor issue due to the difficulty associated with selective dry etching of these materials at the nanoscale. For this reason, the development of new synthetic routes to grow SrTiO₃ nanostructures with good control of the crystal lattice and morphology is of great technological importance.

SrTiO₃ thin films have been prepared on Si substrates by several vacuum techniques, such as molecular beam epitaxy (MBE),^{10–16} sputtering,²¹ pulsed laser ablation,²² physical vapour deposition (PVD)²³ and electron-cyclotron-resonance ion beam sputter deposition.²⁴ A deep understanding on the growth mechanisms, interfacial layer properties and the effect of buffer layers on the structure of SrTiO₃ has been achieved through the use of these techniques. Solution-based methods, based on metalorganic decomposition (MOD) processes offer a versatile and low-cost alternative to vacuum techniques, as they are capable of producing crystalline deposits of a wide range of perovskite materials on large areas with uniform composition and thickness.^{25–28} A typical MOD process involves

^aInstituto de Ciencia de Materiales de Madrid, CSIC, C/Sor Juana Inés de la Cruz 3, 28049 Madrid, Spain. E-mail: ptejedor@icmm.csic.es

^bDepartamento de Física, Universidad Carlos III de Madrid, C/Butarque 15, 28911 Leganés, Spain

the dissolution of metalorganic compounds, which contain the precursor species, in a common solvent, and the subsequent coating of a substrate with the solution using a liquid phase film growth technique, such as spin coating. This is followed by heating of the wet films at increasing temperatures to remove the solvent, to induce the pyrolysis of the metalorganic precursors, and to crystallize the resulting inorganic film, successively.

Previous studies have shown that epitaxial growth of SrTiO_3 thin films on Si (001) substrates proceeds *via* a two-dimensional (2D) layer-by-layer or Frank-van der Merwe (FM) growth mechanism.¹² But for the realization of nanostructures in this system the experimental conditions have to be chosen to induce the growth of three-dimensional (3D) islands directly on the substrate *via* a Volmer-Weber (VW) mechanism.¹⁶ In this article, we describe a novel MOD process based on the utilization of highly diluted solutions of a single metalorganic precursor, $\text{SrTi}(\text{OC}_3\text{H}_7)_6$, and rapid thermal annealing (RTA) that allows the formation of 3D islands, nanorings or atomically smooth thin films of SrTiO_3 on Si substrates by tuning the main experimental parameters, *i.e.*, precursor solution concentration and crystallization temperature. In the following, we study by atomic force microscopy the island/ring size distribution and density, derive the critical nucleus size and discuss the mechanisms that control the formation of the various nanostructures in the SrTiO_3/Si system. We will also show, based on the characterisation by infrared spectroscopy and transmission electron microscopy, that the SrTiO_3 islands grow commensurately strained on the Si substrate with analogous structural characteristics to ultrathin films deposited by conventional epitaxial techniques.

Experimental

A commercial strontium-titanium isopropoxide ($\text{SrTi}(\text{OC}_3\text{H}_7)_6$, 5.15% wt/vol solution (Multivalent Laboratory, UK) in isopropanol ($\text{C}_3\text{H}_7\text{OH}$) (JT Baker® 9079-05 CMOS grade) that was further diluted in the same solvent was used as the precursor solution. Unlike previous methods employed to prepare SrTiO_3 thin films by MOD, our method uses only one metalorganic precursor which contains both Sr and Ti metals, which favours the formation of a single stoichiometric phase.²⁹ The commercial ($\text{SrTi}(\text{OC}_3\text{H}_7)_6$) solution was homogenised in an ultrasonic bath for 12 hours prior to its dilution in isopropanol. All dilutions were carried out in a glove box under Ar atmosphere to obtain final concentrations that ranged between 1.0×10^{-3} and 9.0×10^{-3} M. The filtered (0.2 μm pore diameter) precursor solutions were subsequently deposited onto $10 \times 10 \text{ mm}^2$ Si (001) substrates by spin coating during 45 s at 2000 RPM in air. The Si substrates were previously dipped in a 1 : 1 HF- H_2O solution and rinsed with distilled H_2O to eliminate the Si surface native oxide. The as-deposited films were then heated to 120–150 °C in air for 10–20 min to evaporate the solvent. Subsequently, the temperature was gradually increased to 350–400 °C and kept constant for 30 min to facilitate the pyro-

lysis of the precursor species. After the decomposition treatment, the films were crystallized in a Jipelec-JetStar100 T rapid thermal annealing furnace, by heating the samples to 750 °C for 2 min (series 1) or to 800 °C during 4 min (series 2) under flowing O_2 . The rapid thermal processing (RTP) minimizes the oxidation of the Si surface by reaction with the substrate, which can be significant when the samples are processed for several hours in conventional tube furnaces under O_2 ambient. The heating-cooling ramps selected for the RTP process consisted of the following steps: (1) vacuum (60 s), (2) O_2 input (120 s), (3) heating from RT to 750/800 °C at 30 °C s^{-1} , (4) heating at 750–800 °C during 2–4 min, and (5) cooling ramp from 750/800 °C to RT at 30 °C s^{-1} . All the preparation process was carried out in a clean room.

The morphological characterization of the samples was performed with a Nanoscope IIIa (Veeco, USA) atomic force microscope operating in dynamic mode. As probes we used crystalline Si cantilevers having a nominal spring constant of $\approx 40 \text{ N m}^{-1}$ and a resonance frequency in the 250–330 kHz range. The tip nominal radius was 8 nm. The imaging scan rate was 0.5–2 Hz and the data acquisition was carried out at 512 points per scan line. The samples were imaged at different locations using different tips. It is important to mention that the lateral size values cannot be determined with the same accuracy as the height values, given the unavoidable convolution effects of the tip present in all AFM measurements, a circumstance that is particularly relevant for nanoscale-size features.³⁰

The composition of the SrTiO_3/Si samples was analysed with the aid of a Nicolet 20SXC attenuated total reflectance Fourier transform infrared (ATR-FTIR) spectrophotometer. The crystal structure of the deposits was investigated by high-resolution transmission electron microscopy (HR-TEM) using a Philips Tecnai 20 TEM operating at 200 keV. Cross-sectional specimens for TEM examination were prepared with a focused ion beam (FIB) FEI Quanta FEG dual-beam system.

Results and discussion

The precursor solution concentration and the crystallization temperature were the main parameters controlling the size, shape and density of oxide nanostructures deposited by MOD on planar substrates. Studying the island statistics provided useful information relative to their nucleation and growth kinetics. When using precursor solution concentrations of 1×10^{-3} M the deposits annealed at 650 °C led to the nucleation of three-dimensional (3D) islands in coexistence with an intermediate phase of conformationally disordered macromolecules derived from the $\text{SrTi}(\text{OC}_3\text{H}_7)_6$ precursor (not shown here), which presumably had not been completely decomposed during the RTA process. At concentrations above 1.0×10^{-2} M, this intermediate phase was not observed on the surface, and continuous films with a r.m.s. roughness of 2 nm were formed instead. Since the formation of SrTiO_3 nanostructures was not favoured within the solution concentration range studied, annealing experiments at this low temperature

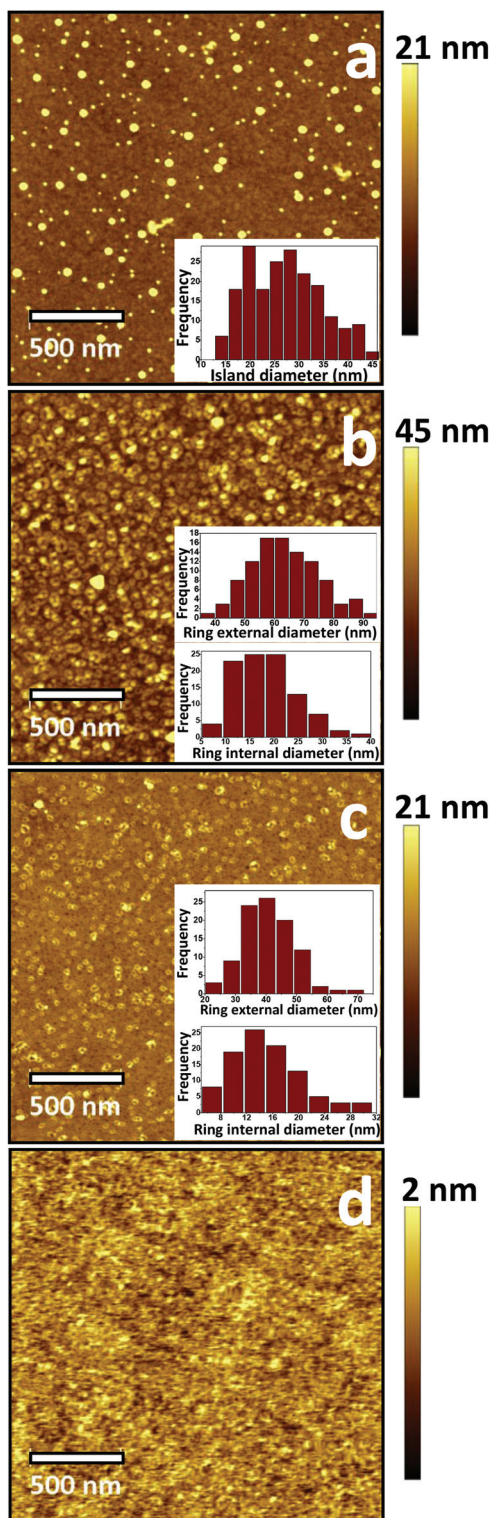


Fig. 1 The surface morphology evolution of SrTiO_3 with $\text{SrTi}(\text{OC}_3\text{H}_7)_6$ concentration for a crystallization temperature of 750°C : (a) 1×10^{-3} M, (b) 3×10^{-3} M (c) 7×10^{-3} M and (d) 1×10^{-2} M. The insets show the size distribution histograms of the SrTiO_3 nanostructures formed in each case. The bin size in each case has been chosen to reflect the mono- or bimodal character of the ring/island distribution observed in the image. Note the different vertical scale for each image.

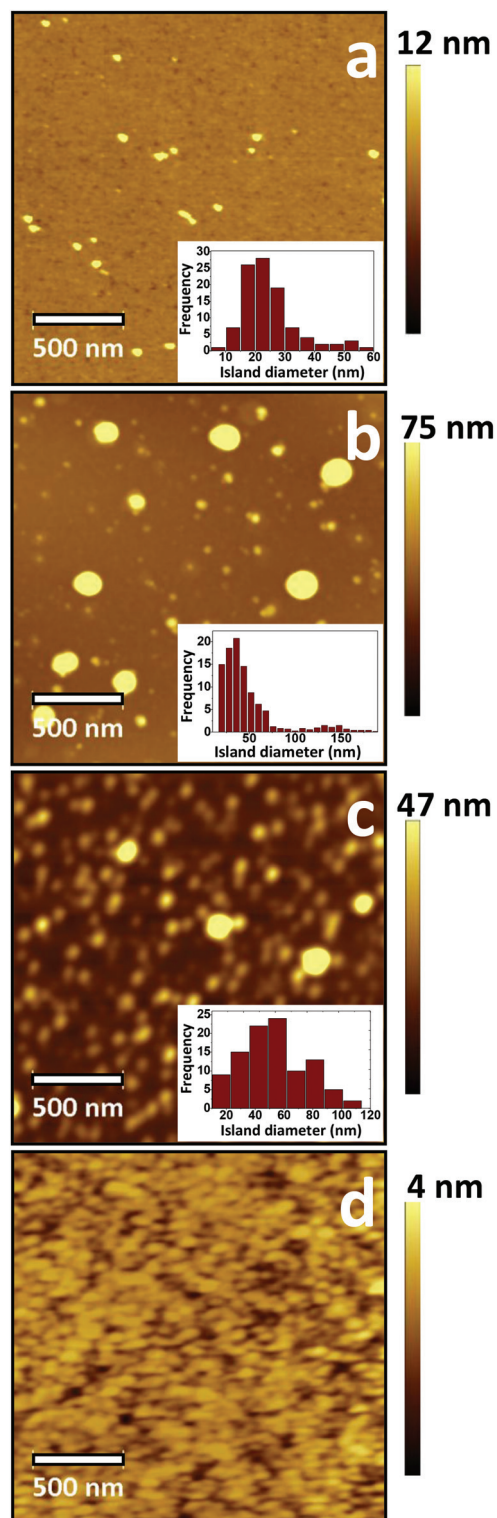


Fig. 2 The surface morphology evolution of SrTiO_3 with $\text{SrTi}(\text{OC}_3\text{H}_7)_6$ concentration for a crystallization temperature of 800°C : (a) 1×10^{-3} M, (b) 3×10^{-3} M (c) 7×10^{-3} M and (d) 1×10^{-2} M. The insets show the size distribution histograms of the SrTiO_3 islands. The bin size in each case has been chosen to reflect the bimodal character of the island size distribution observed in the image. Note the different vertical scale for each image.

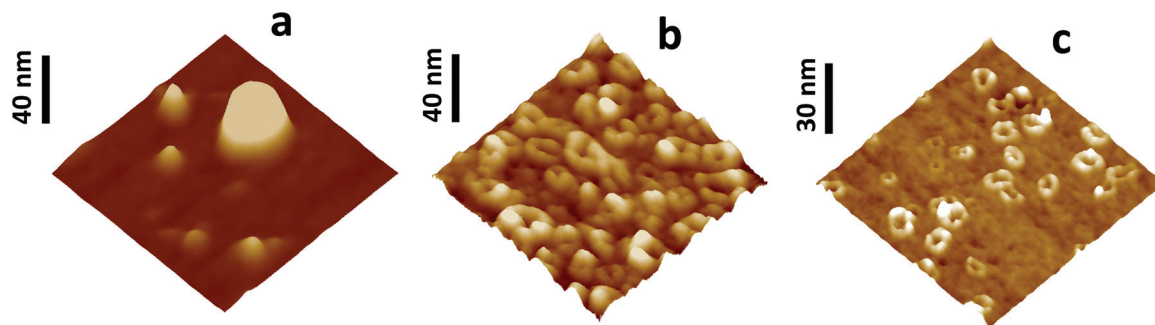


Fig. 3 Three-dimensional AFM images of SrTiO₃ nanostructures grown on Si (001) under different precursor concentration and temperature conditions: (a) 3×10^{-3} M, 800 °C (image size: 400×400 nm²), (b) 3×10^{-3} M, 750 °C (image size: 380×380 nm²) and (c) 7×10^{-3} M, 750 °C (image size: 320×320 nm²).

were not pursued further. By contrast, the deposits crystallized at 750 °C revealed the formation of 3D islands at 1×10^{-3} M and densely-packed rings from a concentration of 3×10^{-3} M onwards. At concentrations above 1×10^{-2} M the formation of continuous films was observed, as depicted in the AFM topography images gathered in Fig. 1(a)–(d). At the crystallization temperature of 800 °C, only 3D islands were observed, whose density initially increased with precursor solution concentration and decreased for concentrations above 3×10^{-3} M, due to coalescence and film formation (r.m.s. roughness = 2–4 nm), as shown in Fig. 2(a)–(d). The 3D AFM images depicted in Fig. 3(a)–(c) show in more detail the morphology of the SrTiO₃ islands and rings formed on Si. At higher crystallization temperatures, *i.e.* 900 °C, only continuous films were formed in the concentration range here studied.

The insets in Fig. 1 and 2 are the size distribution histograms of the SrTiO₃ nanostructures formed in each particular sample, extracted from 100–200 AFM cross-section profiles randomly measured across 1.0×1.0 μm² images. The bin size in each histogram was chosen to reflect the mono- or bimodal character of the island/ring distribution observed in the images. Regardless of annealing temperature, 3D islands exhibit a bimodal distribution, which agrees qualitatively with the cluster size distribution predicted by Venables³¹ for dominant growth-induced coalescence. The interactions between the SrTiO₃ precursor species are stronger than the interactions between these species and the Si substrate.³² This leads to a Volmer–Weber growth mode in which the Sr–O and Ti–O containing species, released during the pyrolysis step, migrate on the Si surface and remain unstable until the smallest critical nucleus size (*i*) is reached. Stable clusters, according to the size distribution observed, are immobile and coalesce as their growing edges merge together. By contrast, nanorings formed at 750 °C exhibit a monomodal size distribution generally associated with a dynamic coalescence, characteristic of mobile clusters that grow together upon impact.^{33,34} The dependence of surface fractional coverage (θ) on solution concentration (*C*) at different temperatures also evidences this change in coalescence mechanism, as depicted in the log-log plot shown in Fig. 4: three-dimensional islands form at low concentrations, following a $\theta \sim C^2$ power law dependence,

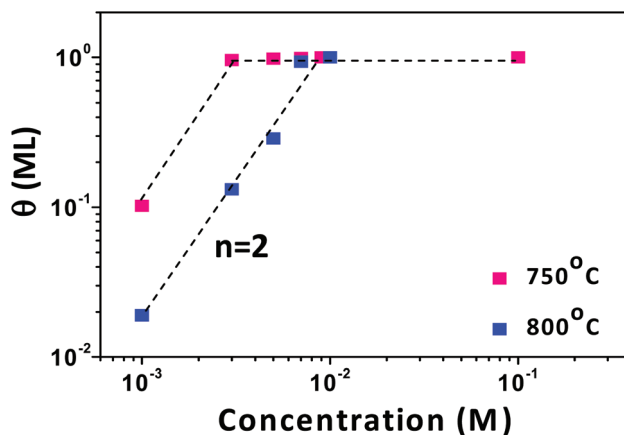


Fig. 4 The dependence of surface fractional coverage on precursor solution concentration at different RTA temperatures.

whereas the onset of nanoring formation appears to be favoured by higher supersaturation conditions and occurs near the coalescence regime, where the surface coverage depends very weakly on concentration. The variation of nanostructure diameter, height and density respectively with solution concentration for the two annealing temperatures studied is illustrated in Fig. 5(a)–(c). All three parameters increase with concentration in the nucleation regime up to a value of $3\text{--}5 \times 10^{-3}$ M and decay rapidly above this value. Once a layer has been completed, new islands nucleate and the coalescence process starts again.

The nucleation density behaviour is qualitatively similar for both temperatures and has the general form expected for critical nucleus sizes greater than 1 (*i* > 1), and single adatom capture.³⁵ We can distinguish in Fig. 5(c) the low-coverage regime dominated by island nucleation, where the island density increases rapidly with concentration. In this regime the creation of nuclei in favourable lattice sites is the controlling step. The coalescence regime is observable at higher concentrations, where the island density decreases rapidly to form a continuous film. The critical nucleus size has been calculated from the dependence of the island density (*N*) on the deposition rate (*F*), given by the longstanding Venables' equation $N \approx F^{1/(i+2)}$.^{36,37} Fig. 6 shows the log-log plot of the

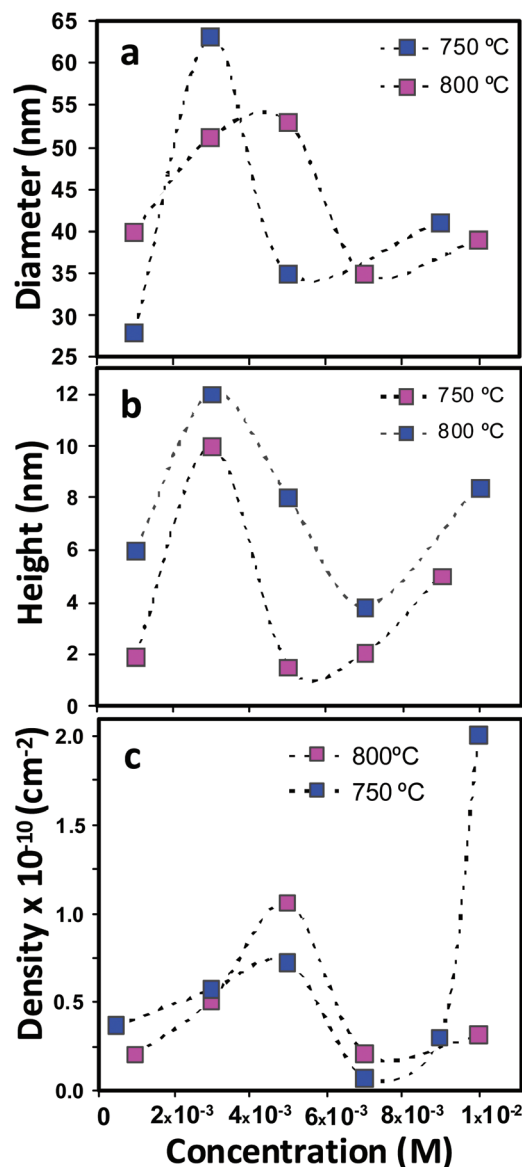


Fig. 5 The dependence of SrTiO₃ nanostructure diameter (a), height (b) and density (c) on precursor concentration at different RTA temperatures. The data were extracted from AFM images recorded at a scan rate of 0.5–2 Hz with 512 points per scanline.

island density *versus* the growth rate, determined from the surface fractional coverage attained at a given processing time for the 800 °C experimental series. The dotted line represents the best fit to a power law dependence and yields an exponent of 0.6, *i.e.*, $i = 3$, corresponding to a smallest stable island formed by 4 atoms.

Although the formation of SrTiO₃ nanorings on Si substrates had not been previously reported, the spontaneous transformation of 3D islands (nanoclusters) into nanorings as a strain-relief mechanism is well documented in the literature for other heterostructural systems, such as InAs/GaAs,^{38,39} Si/Ge⁴⁰ and Au/indium-tin-oxide (ITO).⁴¹ Such transformation has been explained in terms of a preferential migration of precursor species from the top of the strained island towards the

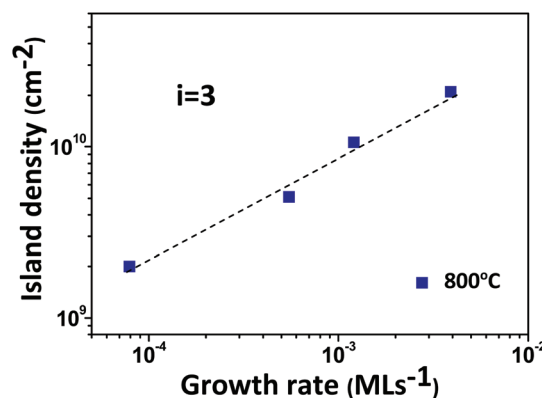


Fig. 6 Log–log plot of the SrTiO₃ island density vs. growth rate for a RTA temperature of 800 °C. The critical nucleus size derived from the Venables³⁶ fit corresponds to a trimer.

island base, where adatom incorporation is more favourable. The island-to-ring transition has been also analysed in a recent energetic model proposed by Gill,⁴² which establishes that nanoclusters are thermodynamically more stable than nanorings. But when nanoclusters reach a certain diameter they can undergo a barrierless transformation into nanorings to reduce the elastic strain energy by increasing their slope. The rate of this process depends on the size of the nanocluster and its initial morphology and slope. It is worth noting here that the AFM profiles extracted from Fig. 1 and 2 revealed that the walls of the nanorings prepared at 750 °C were steeper than those of the 3D islands annealed at 800 °C, in good agreement with the predictions of Gill's model. Notwithstanding, the evolution of the SrTiO₃ morphology with concentration observed at different temperatures, illustrated schematically in Fig. 7, suggests that the process is also affected by kinetics. When the adatom population in the surface is relatively low, that is, at low solution concentrations or high substrate temperatures, the Sr–O and Ti–O precursor species tend to migrate from the surface toward the top surface of a growing island, where they incorporate preferentially. But when the precursor concentration is raised at lower temperatures, the adatom population is much higher and the island size reaches rapidly the critical size for the island-to-ring transformation, as we observe at 750 °C for concentrations $\geq 3 \times 10^{-3}$ M. At 800 °C, given that the adatom mobility and the attachment to island edges is faster, the growing islands coalesce laterally before they can attain the critical diameter required to undergo the island-to-ring transition.

Chemical phase analysis of the SrTiO₃ deposits by ATR-FTIR spectroscopy required the preparation of thicker films (≈ 20 nm) using a multi-layer spin coating approach. To this aim, three layers were deposited on a Si substrate from a 1.0×10^{-2} M precursor solution by consecutive repetition of the spinning and drying steps, followed by crystallization at 800 °C. In Fig. 8 we present the FTIR spectrum of the film in the 400–1500 cm⁻¹ range. The main bands observed in the low-energy region of the spectrum are associated with vibrations of the TiO₆ octahedra in SrTiO₃.^{43,44} The peak at

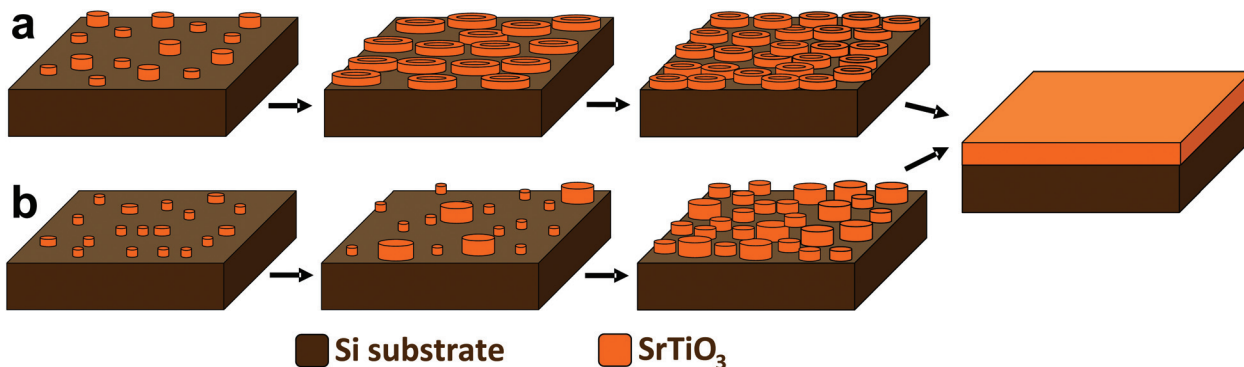


Fig. 7 Schematic drawing of the SrTiO₃ morphology evolution with precursor concentration at 750 °C (a) and 800 °C (b), respectively.

450 cm⁻¹ (E_u phonon) and an intense band at 600 cm⁻¹ (A_{2u} + E_u phonon) evidence the formation of the tetragonal phase by rotation of the TiO₆ octahedra around the *c* axis in the compressively strained film, in good agreement with previously reported theoretical calculations⁴⁵ and strain-temperature phase diagrams derived from X-ray measurements of epitaxial SrTiO₃.⁴⁶ All other bands observable in the spectrum can be assigned to a mixed Sr/Ti silicate with different degrees of polymerization and numbers of non-bridging oxygens per silicon (NBO/Si) in the anionic structural units, [SiO₄]⁴⁻.^{47–49} This phase is generally present as an interfacial layer, formed by reaction of the SrTiO₃ film with the underlying Si substrate during high temperature annealing: The rocking (overlapped with the O–Ti–O bending mode) and bending modes of Si–O bonds can be observed at 470 cm⁻¹ and 560 cm⁻¹, respectively. The absorptions at 740 cm⁻¹ and 770 cm⁻¹ are assigned to the stretching vibration modes of [Si₃O₉]⁶⁻-rings and [Si₂O₇]⁶⁻-dimers, while the bands located in the 800–1200 cm⁻¹ region correspond to the stretching vibrations of [SiO₄]⁴⁻ tetrahedra. Specifically, the weak peak at 820 cm⁻¹ is attributed to symmetric M–O–Si stretching vibrations, where M can be a Si, Ti or Sr atom and the wide band at 910 cm⁻¹ includes Si–O stretching modes of defective silicate units having 3 or 4 NBO/Si. In addition, the shoulder at 960 cm⁻¹ is assigned to the out-of plane asymmetric stretching of the four connected Ti/Sr–O–Si oscillators (equivalent to the out-of phase stretching of the four Si–O bonds pointing toward the Ti/Sr atoms) and the wide band at ≈1120 cm⁻¹ is assigned to the in-phase stretching of four Si–O bonds surrounding a Ti/Sr atom. Finally a weak absorption is observed at 1285 cm⁻¹, attributable to the asymmetric stretching of fully polymerized SiO₄ units (NBO/Si = 0).

The structural properties of the SrTiO₃ nanostructures were examined by TEM analysis. Fig. 9(a) and 9(b) are cross-sectional bright-field high-resolution images taken with different magnifications of an island deposited on a Si (001) substrate from a 5 × 10⁻³ M precursor solution and subsequently annealed at 800 °C. The images revealed that the ≈25 nm diameter island is monocrystalline and appears to sit on a ≈1.5 nm thick interfacial layer, which based on the FTIR analysis of the SrTiO₃ thin film presented above is likely to be

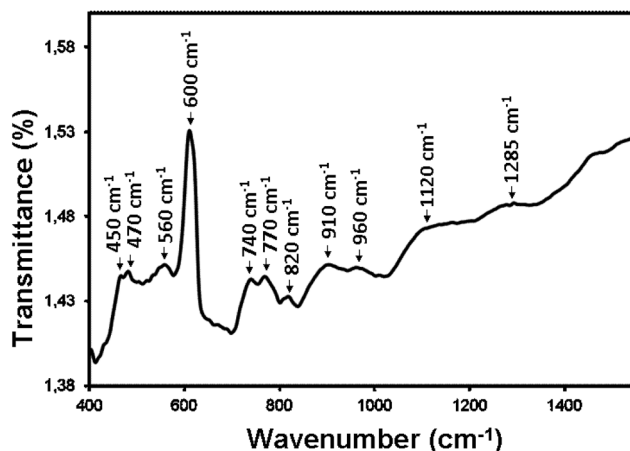


Fig. 8 ATR-FTIR spectrum of a 20 nm-thick SrTiO₃ film deposited on Si(001) from a 10⁻² M SrTi(OC₃H₇)₆ solution and crystallized by RTA at 800 °C.

formed by a mixed Sr/Ti silicate. The island is covered with a thin Pt film, deposited to protect the sample during FIB cross-sectioning.

The fast Fourier transform (FFT) pattern corresponding to the image in Fig. 9(b), which was taken with the incident electron beam parallel to the [110] direction of the Si substrate, can be seen in Fig. 9(c). In addition to the diffuse rings that stem from the amorphous Pt film, we observe intense diffraction spots that can be indexed as 200 and 110 reflections of the high temperature, high symmetry tetragonal (*P4/mmm*) SrTiO₃ phase.⁴⁶ The calculated in-plane and out-of-plane lattice parameters of SrTiO₃ are *a*_{||} (*a*) = 3.754 Å and *a*_⊥ (*c*) = 4.043 Å, respectively. This results in a tetragonality (*c/a* – 1) value of 0.07, only slightly larger than that of MBE-grown SrTiO₃ film of similar thickness.⁵⁰

The in-plane compressive strain, defined as $\epsilon = (a_{||} - a_o)/a_o$, where *a*_o is the lattice parameter of bulk SrTiO₃ (0.3905 nm) is –3.86%. The island is thus strained commensurately to the underlying Si substrate and expanded in the perpendicular direction, which coincides with the axis of rotation of the TiO₆ octahedra. The epitaxial orientation relationship is (001) SrTiO₃//(001)Si and [100]SrTiO₃//[110]Si, that is, the SrTiO₃

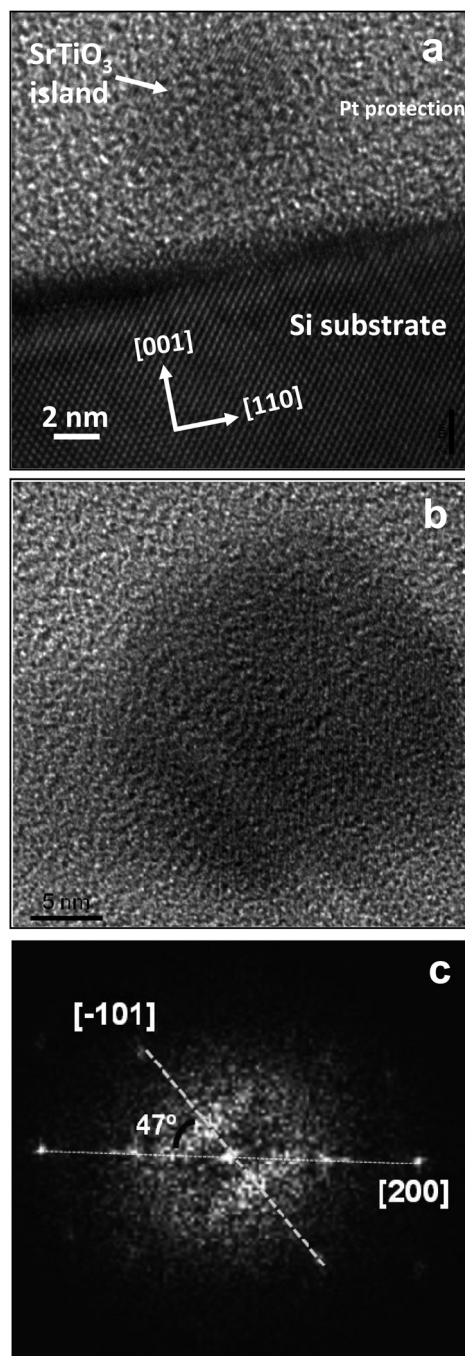


Fig. 9 Cross-section HR-TEM micrographs of an SrTiO_3 island deposited on a Si substrate from a 5×10^{-3} M precursor solution and crystallized at 800 °C, taken at different magnifications (a–b) and Fast Fourier Transform (FFT) (c) of the image in (b), equivalent to the experimental electron diffraction pattern of the island.

lattice is rotated 45° on the (001) Si surface, so that a $\langle 100 \rangle$ direction in SrTiO_3 is aligned with a $\langle 110 \rangle$ direction in Si. The angle value of 47° measured from the FFT pattern suggests a slight misalignment of the SrTiO_3 lattice with respect to Si substrate (mosaicity), also observed in tetragonal SrTiO_3/Si thin films grown by MBE. Our results thus show that the nanostructures prepared with the synthetic route presented here

have similar structural characteristics to films with the same thickness grown by conventional epitaxial techniques and consequently have the potential to exhibit ferroelectric behavior. An issue to be addressed in future studies is the optimization of the O_2 flux¹⁵ used during the RTA process to minimize the interfacial layer thickness.

Conclusions

In conclusion, thermal decomposition of diluted solutions of $\text{SrTi}(\text{OC}_3\text{H}_7)_6$, used as single metalorganic precursor, offers a low-cost and controllable route to deposit SrTiO_3 3D islands and nanorings on Si substrates. The deposition process has been studied as a function of precursor solution concentration and crystallization temperature by quantitative analysis of AFM images, showing the existence of a nucleation regime for concentrations $\leq 5 \times 10^{-3}$ M and a coalescence regime above this value. The study of the island density evolution with concentration has revealed that the critical nucleus size corresponds to a trimer. In addition, the island-size distributions exhibit a bimodal behavior, characteristic of a process where coalescence is dominated by the lateral growth of immobile clusters, in contrast with the dynamical coalescence found for nanorings. The formation of nanorings with average sizes above a critical value occurs under high supersaturation conditions to reduce the elastic strain energy generated by the lattice mismatch between the nanostructure and the Si substrate. The nanoclusters prepared by this novel process are single-crystalline and compressively strained, resulting in a tetragonal SrTiO_3 phase structurally comparable to that present in epitaxial thin films that exhibit ferroelectric behavior, thus offering good prospects for the fabrication of nanoscale memory and field effect transistor devices. Moreover, since SrTiO_3 exhibits piezoelectricity and superconductivity at low-temperatures, the newly reported nanorings could have applications in sensors, resonators and transducers.

Acknowledgements

Financial support from Spanish MICINN under grants MAT2011-22536 and FIS2012-38866-C05-05 is gratefully acknowledged. The authors are indebted to M.L. Calzada and I. Bretos for technical assistance with the clean-room equipment used in this work.

Notes and references

- 1 J. M. Rondellini, S. J. May and J. W. Freeland, *Mater. Res. Bull.*, 2012, **37**, 261.
- 2 J. H. Haeni, P. Irvin, W. Chang, R. Uecker, P. Reiche, Y. L. Li, S. Choudhury, W. Tian, M. E. Hawley, B. Craigo, A. K. Tagantsev, X. Q. Pan, S. K. Streiffer, L. Q. Chen, S. W. Kirchoefer, J. Levy and D. G. Schlom, *Nature*, 2004, **430**, 758.

- 3 K. Iwashina and A. Kudo, *J. Am. Chem. Soc.*, 2011, **133**, 13272.
- 4 H.-C. Chen, C.-W. Huang, J. C. S. Wu and S.-T. Lin, *J. Phys. Chem. C*, 2012, **116**, 7897.
- 5 X. B. Yan, K. Li, J. Jin, Y. D. Xia, H. X. Guo, L. Chen and Z. G. Liu, *Electrochem. Solid-State Lett.*, 2010, **13**, H87.
- 6 R. Waser and M. Aono, *Nat. Mater.*, 2007, **6**, 833.
- 7 H. Y. Hwang, Y. Iwasa, M. Kawasaki, B. Keimer, N. Nagaosa and Y. Tokura, *Nat. Mater.*, 2012, **11**, 103.
- 8 A. Annadi, Q. Zhang, X. R. Wang, N. Tuzla, K. Gopinadhan, W. M. Lü, A. Roy Barman, Z. Q. Liu, A. Srivastava, S. Saha, Y. L. Zhao, S. W. Zeng, S. Dhar, E. Olsson, B. Gu, S. Yunoki, S. Maekawa, H. Hilgkamp, T. Venkatesan and Ariando, *Nat. Commun.*, 2013, **4**, 1838.
- 9 M. Boucherit, O. F. Shoron, T. A. Cain, C. A. Jackson, S. Stemmer and S. Rajan, *Appl. Phys. Lett.*, 2013, **102**, 242909.
- 10 C. J. Först, C. R. Ashman, K. Schwarz and P. E. Blöchl, *Nature*, 2004, **427**, 53.
- 11 J. W. Reiner, A. M. Kolpak, Y. Segal, K. F. Garrity, S. Ismail-Beigi, C. H. Ahn and F. J. Walker, *Adv. Mater.*, 2010, **22**, 2919.
- 12 R. Droopad, Z. Yu, J. Ramdani, L. Hilt, J. Curless, C. Overgaard, J. L. Edwards Jr., J. Finder, K. Eisenbeiser and W. Ooms, *Mater. Sci. Eng., B*, 2001, **87**, 292.
- 13 L. F. Kourkoutis, C. S. Hellberg, V. Vaithyanathan, H. Li, M. K. Parker, K. E. Andersen, D. G. Schlom and D. A. Muller, *Phys. Rev. Lett.*, 2008, **100**, 036101.
- 14 M. P. Warusawithana, C. Cen, C. R. Slesman, J. C. Woicik, Y. Li, L. F. Kourkoutis, J. A. Klug, H. Li, P. Ryan, L.-P. Wang, M. Bedzyk, D. A. Muller, L.-Q. Chen, J. Levy and D. G. Schlom, *Science*, 2009, **324**, 367.
- 15 G. Niu, W. W. Peng, G. Saint-Girons, J. Penuelas, P. Roy, J. B. Brubach, J.-L. Maurice, G. Hollinger and B. Vilquin, *Thin Solid Films*, 2011, **519**, 5722.
- 16 F. Niu and B. W. Wessels, *J. Cryst. Growth*, 2007, **300**, 509.
- 17 S. Salahuddin and S. Datta, *Nano Lett.*, 2008, **8**, 405.
- 18 V. V. Zhirnov and R. K. Cavin, *Nat. Nanotechnol.*, 2008, **3**, 77.
- 19 G. Saint-Girons, J. Cheng, P. Regreny, L. Largeau, G. Patriarche and G. Hollinger, *Phys. Rev. B: Condens. Matter*, 2009, **80**, 155308.
- 20 A. Antons, J. B. Neaton, K. M. Rabe and D. Vanderbilt, *Phys. Rev. B: Condens. Matter*, 2005, **71**, 024102.
- 21 H. J. Bian, X. F. Chen, J. S. Pan, W. Zhu and C. Q. Sun, *Appl. Surf. Sci.*, 2010, **255**, 4867.
- 22 P. Tejedor, V. M. Fuenzalida and F. Briones, *J. Appl. Phys.*, 1996, **80**, 799.
- 23 T. Q. Ngo, A. Posadas, M. D. McDaniel, D. A. Ferrer, J. Bruley, C. Breslin, A. A. Demkov and J. G. Ekerdt, *J. Cryst. Growth*, 2013, **363**, 150.
- 24 G. Panomsuwan, O. Takai and N. Saito, *J. Am. Ceram. Soc.*, 2014, **97**, 1383.
- 25 P. Tejedor, C. Ocal, E. Barrena, R. Jiménez, C. Alemany and J. Mendiola, *J. Electrochem. Soc.*, 2002, **149**, 1.
- 26 P. Tejedor, A. B. Fernández, R. Jiménez, C. Alemany and J. Mendiola, *Microelectron. Reliab.*, 2000, **40**, 683.
- 27 X. Wang, X. Lu, H. Bo, Y. Liu, Y. Shen, X. Wu, W. Cai, Y. Kan, C. Zhang, Y. Liu, F. Huang and J. Zhu, *Solid State Commun.*, 2010, **150**, 1637.
- 28 E. Gutmann, A. A. Levin, M. Reibold, J. Müller, P. Paufler and D. C. Meyer, *J. Solid State Chem.*, 2006, **179**, 1864.
- 29 K. W. Kirby, *Mater. Res. Bull.*, 1988, **23**, 881.
- 30 C. Odin, J. P. Aimé, Z. El Kaakour and T. Bouhacina, *Surf. Sci.*, 1994, **317**, 321.
- 31 J. A. Venables, *Thin Solid Films*, 1976, **32**, 135.
- 32 R. Thomas, R. Bhakta, P. Ehrhart, R. A. Fischer, R. Waser and A. Devi, *Surf. Coat. Technol.*, 2007, **201**, 9135.
- 33 J. A. Venables, G. D. T. Spiller and M. Hanbücken, *Rep. Prog. Phys.*, 1984, **47**, 399.
- 34 M. Zinke-Allmann, L. C. Feldman and M. H. Grabow, *Surf. Sci. Rep.*, 1992, **16**, 377.
- 35 J. G. Amar and F. Family, *Phys. Rev. Lett.*, 1995, **74**, 2066.
- 36 J. A. Venables, *Philos. Mag.*, 1973, **27**, 697.
- 37 I. Doudevski and D. K. Schwartz, *J. Am. Chem. Soc.*, 2001, **123**, 6867.
- 38 J. M. Garcia, G. Medeiros-Ribeiro, K. Schmidt, T. Ngo, J. L. Feng, A. Lorke, J. Kotthaus and P. M. Petroff, *Appl. Phys. Lett.*, 1997, **71**, 2014.
- 39 T. Raz, D. Ritter and G. Bahir, *Appl. Phys. Lett.*, 2003, **82**, 1706.
- 40 M. Stoffel, A. Malachias, A. Rastelli, T. H. Metzger and O. G. Schmidt, *Appl. Phys. Lett.*, 2009, **94**, 253114.
- 41 F. Ruffino, I. Crupi, F. Simone and M. G. Grimaldi, *Appl. Phys. Lett.*, 2011, **98**, 023101.
- 42 S. P. A. Gill, *J. Appl. Phys.*, 2013, **113**, 154316.
- 43 S. Keshri, L. Joshi and S. S. Rajput, *J. Alloys Compd.*, 2011, **509**, 5796.
- 44 N. Zhou, G. Chen, H. J. Zhang and C. Zhou, *J. Alloys Compd.*, 2009, **477**, L17.
- 45 R. A. Evarestov, E. Blokhin, D. Gryaznov, E. A. Kotomin and J. Maier, *Phys. Rev. B: Condens. Matter*, 2011, **83**, 134108.
- 46 F. He, B. O. Wells and S. M. Saphiro, *Phys. Rev. Lett.*, 2005, **94**, 176101.
- 47 J. H. Park, D. J. Min and H. S. Song, *ISIJ Int.*, 2002, **42**, 344.
- 48 G. Ricchiardi, A. Damin, S. Bordiga, C. Lamberti, G. Spano, F. Rivetti and A. Zecchina, *J. Am. Chem. Soc.*, 2001, **123**, 11409.
- 49 Y. Hu, W. Zhuang, J. Hao, X. Huang and H. He, *Open J. Inorg. Chem.*, 2012, **2**, 6.
- 50 G. Niu, J. Penuelas, L. Largeau, B. Vilquin, J. L. Maurice, C. Botella, G. Hollinger and G. Saint-Girons, *Phys. Rev. B: Condens. Matter*, 2011, **83**, 054105.